

# **Progress Report on the Assessment of the Material Performance for TCR Applications**

---

**Nuclear Science and Engineering Division**

### **About Argonne National Laboratory**

Argonne is a U.S. Department of Energy laboratory managed by UChicago Argonne, LLC under contract DE-AC02-06CH11357. The Laboratory's main facility is outside Chicago, at 9700 South Cass Avenue, Argonne, Illinois 60439. For information about Argonne and its pioneering science and technology programs, see [www.anl.gov](http://www.anl.gov).

### **DOCUMENT AVAILABILITY**

**Online Access:** U.S. Department of Energy (DOE) reports produced after 1991 and a growing number of pre-1991 documents are available free at OSTI.GOV (<http://www.osti.gov>), a service of the US Dept. of Energy's Office of Scientific and Technical Information.

### **Reports not in digital format may be purchased by the public from the National Technical Information Service (NTIS):**

U.S. Department of Commerce  
National Technical Information Service  
5301 Shawnee Rd  
Alexandria, VA 22312  
**[www.ntis.gov](http://www.ntis.gov)**  
Phone: (800) 553-NTIS (6847) or (703) 605-6000  
Fax: (703) 605-6900  
Email: [orders@ntis.gov](mailto:orders@ntis.gov)

### **Reports not in digital format are available to DOE and DOE contractors from the Office of Scientific and Technical Information (OSTI):**

U.S. Department of Energy  
Office of Scientific and Technical Information  
P.O. Box 62  
Oak Ridge, TN 37831-0062  
**[www.osti.gov](http://www.osti.gov)**  
Phone: (865) 576-8401  
Fax: (865) 576-5728  
Email: [reports@osti.gov](mailto:reports@osti.gov)

### **Disclaimer**

This report was prepared as an account of work sponsored by an agency of the United States Government. Neither the United States Government nor any agency thereof, nor UChicago Argonne, LLC, nor any of their employees or officers, makes any warranty, express or implied, or assumes any legal liability or responsibility for the accuracy, completeness, or usefulness of any information, apparatus, product, or process disclosed, or represents that its use would not infringe privately owned rights. Reference herein to any specific commercial product, process, or service by trade name, trademark, manufacturer, or otherwise, does not necessarily constitute or imply its endorsement, recommendation, or favoring by the United States Government or any agency thereof. The views and opinions of document authors expressed herein do not necessarily state or reflect those of the United States Government or any agency thereof, Argonne National Laboratory, or UChicago Argonne, LLC.

# Progress Report on the Assessment of the Material Performance for TCR Applications

---

prepared by  
Meimei Li, Xuan Zhang, Wei-Ying Chen, Florent Heidet  
Nuclear Science and Engineering Division, Argonne National Laboratory

September 2020

## Progress Report on the Assessment of the Material Performance for TCR Applications

Meimei Li, Xuan Zhang, Wei-Ying Chen, Florent Heidet  
Nuclear Science and Engineering Division  
Argonne National Laboratory

### Abstract

The objective of Argonne's materials research activities for the Transformational Challenge Reactor (TCR) program is to improve the understanding of material properties from additive manufacturing with the focus on understanding the creep and fatigue properties of additively manufactured materials. The material work conducted by Argonne provides support in developing and qualifying advanced materials and manufacturing processes to allow for innovative reactor design and licensing for the TCR. In this report, we present the creep data at temperatures of 550, 600 and 650°C and stresses between 175 and 300 MPa for 316L stainless steel produced by a laser powder bed fusion process. We conducted five different post-build heat treatments, namely 650°C/1h, 750°C/1h, 800°C/1h, 900°C/1h and 1050°C/1h. Creep tests of the heat-treated specimens were performed under the same test condition, 550°C/275 MPa to evaluate and understand the effect of post-build heat treatment on the creep behavior of additively-manufactured 316L SS. Creep tests were conducted to ASME NQA-1 or its lab equivalent for quality assurance.

### 1. Introduction

Type 316 austenitic stainless steel has been widely used in various types of nuclear reactors, including current nuclear power plants and next-generation advanced reactor concepts, e.g. sodium-cooled fast reactors, molten-salt reactors, and gas-cooled high temperature reactors. Additive manufacturing as a disruptive manufacturing technology has opened up unprecedented opportunities for designing components with controlled microstructure, enabling smart designs of reactor components with complex geometries, design freedom and possibly enhanced performance [1]. Previous studies have shown that additively-manufactured 316 stainless steel (AM 316 SS) has significantly improved low-temperature tensile strength and good ductility over conventionally-made wrought 316 SS [2-4]. The high-temperature mechanical performance of AM 316 SS is yet to be evaluated and fully understood. A comprehensive database of elevated temperature mechanical properties is needed for its structural applications in the Transformational Challenge Reactor (TCR), a gas-cooled microreactor being developed to demonstrate revolutionary technologies including additive manufacturing [5-7].

Laser powder bed fusion (LPBF) is an additive manufacturing technology whereby laser beams are used to melt and consolidate metal powder lay-by-layer to form parts. It can fabricate complex components with high accuracy that is difficult to achieve by conventional manufacturing techniques, e.g. casting and forging. This new manufacturing technology has seen broad applications in a wide range of industries [8]. Today, austenitic stainless steels are routinely processed by LPBF [9]. The microstructure of LPBF-produced 316 SS is, however, much more complex than that of conventionally-made 316 SS. Various types of defects can be produced during the printing process, such as pores, cracks, etc. [9]. The high-energy input, rapid melting

and solidification process result in a highly non-equilibrium microstructure. As has been observed previously, the microstructure of AM 316 SS has a hierarchical microstructure with length scales spanning several orders of magnitude [3]. A melt pool contains columnar grains within which subgranular cellular structure prevails [10-13]. Solidification cells have diameters of 1  $\mu\text{m}$  or less and have similar crystallographic orientation. Cell walls contain high density dislocations and are segregated with chromium and molybdenum [3]. The cell size is dependent on the thermal gradient and the solidification rate. Rapid solidification has long been recognized as a useful means of producing dislocation substructures. Formation of dendrites and solute segregation resulted from rapid solidification promote the formation of dislocations. Dislocations form cell structure under thermal stress during rapid solidification and cooling by a knitting process involving stress-induced climb [14,15].

The creep behavior of a material is generally determined by (1) material's intrinsic properties e.g. melting temperature, elastic modulus, diffusivity, (2) microstructural features (e.g. grains, subgrains, dislocations, second-phase precipitates), and (3) operating conditions (temperature, stress, environment). Dislocation substructures (cells, subgrains) play an important role in the creep resistance of a material. It should be noted that "dislocation cells" and "subgrains" have been traditionally used to describe the morphologies of dislocation substructures. Dislocation cells often refer to the dislocation substructure consisting of broad, diffused boundaries containing dislocation tangles, while subgrains refer to substructure with narrow and well defined sub-boundaries having a larger misorientation than cell walls. Sometimes these two terms are used interchangeably. In conventionally-made 316 SS, dislocation substructures are widely observed in creep tests at temperatures  $> 700^{\circ}\text{C}$  [16-21]. The influence of subgrain size on creep resistance was also demonstrated by Sherby and Burke [22] that the creep rate of aluminum with a fine subgrain size has higher creep resistance than a material containing coarse subgrains. In AM 316 SS, dislocation cell structure exists before creep tests, and is in fact a structural variable for creep. Little information is available in the literature regarding the creep resistance of AM 316 SS and the roles of the unique microstructural features, e.g. dislocation cells, porosity, solute segregation in the creep response of AM 316 SS.

The work reported here is (1) to evaluate the creep resistance of an LPBF-produced 316L SS (referred to as "AM 316L SS" throughout the report), and (2) to evaluate the effect of post-build heat treatment on the creep properties of AM 316L SS. This assessment is vital to the optimization of process parameters and post-build heat treatment conditions to produce high-quality parts with optimized microstructure and superior properties.

## **2. Experimental**

Creep specimens used in this study were ASTM-standard round bar specimens. Specimens were fabricated from rods of two builds (Build IDs 20190308 and 20190315) of AM 316L SS. Rods were printed by an LPBF process using a Concept Laser-M2 printer at Oak Ridge National Laboratory [23]. Praxair 316L stainless steel powder and default printer settings were used for printing. The chemical composition of 316L feedstock is given in Table 1 [6].

Table 1: Composition of the Praxair 316L stainless steel powder (wt%).

Fe	Cr	Ni	Mo	Mn	Si	N	Cu	Co	C	P	O
Bal.	17.07	12.08	2.41	1.19	0.46	0.01	0.01	0.1	0.006	<0.005	0.05

Printed rods had a nominal diameter of 0.5” and a nominal length of 4.125”. They were printed vertically, and the ID of the rod was printed at the top end of the rod, as shown in Fig. 1. Creep specimens had a nominal gauge diameter of 0.250”, a nominal gauge length of 1.250”, and a total length of 3.60”. One specimen per printed rod was machined. The axial direction of the specimen was along the build direction. The TCR program aims to correlate location-specific *in situ* manufacturing data with post-manufacturing properties [24]. To keep track of the exact location and the build direction of the specimen, the top of the upper grip section of the specimen was aligned with the top of the printed rod, and the upper grip section was designed to be 0.08” longer than the lower grip section of the specimen.

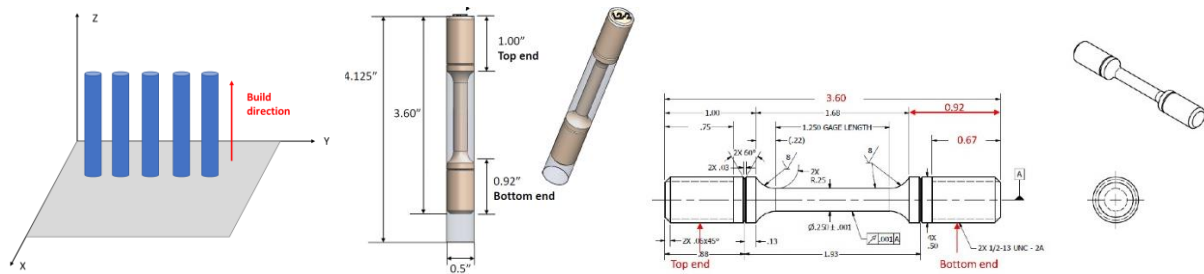


Figure. 1. Specimen fabrication and orientation drawings (all dimensions are in inches).

The Concept Laser – M2 printer uses two identical laser systems in different regions of the powder bed to fabricate larger components. Specimens machined from rods printed by laser 1 were assigned IDs of L1XX and are called “Laser 1 specimens”; specimens machined from rods printed by laser 2 were assigned IDs of L2XX and are called “Laser 2 specimens”. Figure 2 shows the locations of printed rods used for machining “Laser 1 specimens” and “Laser 2 specimens”, respectively, of the build 20190315. This two-laser system enables a direct one-to-one batch variability within a single build while holding all other variables constant.

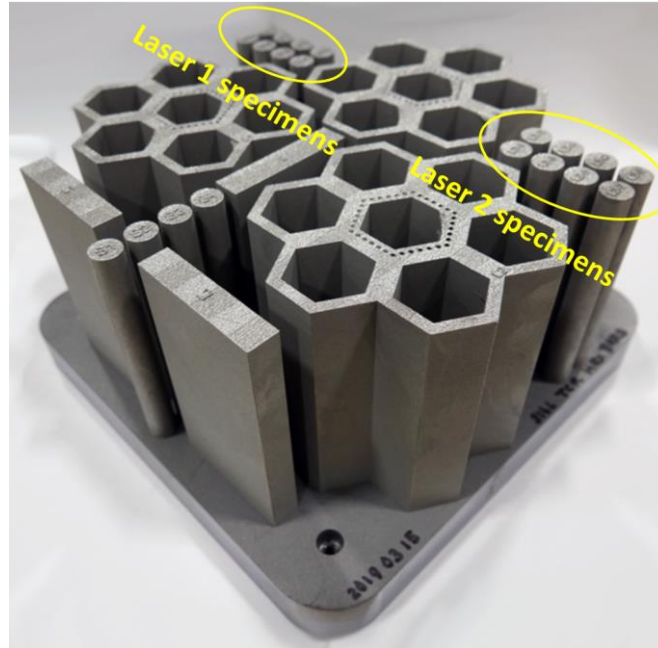


Figure 2. Build 20190315 showing the locations of printed rods used for machining “Laser 1 specimens” and “Laser 2 specimens”, respectively.

Post-build heat treatments were conducted on seven creep specimens at Argonne National Laboratory. Each specimen was individually encapsulated in a quart tube under vacuum. Heat treatments were conducted on the encapsulated specimens in air furnaces. Specimens L106 and L206 were heat treated at 650°C for one hour followed by furnace cooling. Specimens L105 and L205 were heat treated at 1050°C for one hour followed by rapid cooling. Specimens L2-3, L2-4, and L1-4 were heat treated at 750, 800, and 900°C, respectively, for one hour followed by air cooling. All the heat-treated specimens were creep tested under the same condition, namely, 550°C and 275 MPa, to evaluate the effect of post-build heat treatments on the creep behavior of AM 316L SS. Table 2 provides a list of creep specimens and testing conditions of AM 316L SS. Specimen L105 failed during the initial loading to a higher stress of the creep test, and is not included in Table 2.

Creep tests on as-built specimens were conducted at stresses between 175 and 300 MPa and three temperatures, 550, 600, and 650°C ( $0.49 - 0.55 T_m$ , where  $T_m$  is the melting point of 316 SS (1680 K [25])). Several Laser 1 and Laser 2 specimens were tested under the same temperature and stress conditions to evaluate batch variability. Creep tests were conducted according to ASTM Standard E139-11, “Standard Test Methods for Conducting Creep, Creep-Rupture, and Stress-Rupture Tests on Metallic Materials.” Tests were carried out on ATS Series 2300 Lever Arm Creep Testing Systems integrated with WinCCS II computer control and data acquisition software package. Each creep load frame was equipped with a three-zone split-tube furnace capable of operation up to 1100°C (Fig. 3). All specimens were soaked at the test temperature for 1 hour prior to loading to ensure a stable test temperature. The temperature was monitored by 2 thermocouples with each spot-welded to the grip shoulder section of the

specimen. The temperature was maintained to a total variance of  $\pm 1^\circ\text{C}$ . Creep strain was monitored by an averaging extensometer frame mounted on opposite sides of the specimen. Creep elongation was determined by measuring the length of the ruptured specimen. All the specimens were tested to rupture.

Microstructure of a creep specimen in the as-built condition was examined non-destructively before the creep test by synchrotron high-energy X-ray tomography at the beamline 1-ID at the Advanced Photon Source, Argonne National Laboratory. Porosity distribution was measured at the gauge section of the creep specimen by scanning the center region of the gauge with an X-ray energy of 81 keV and a pixel size of  $1.172\ \mu\text{m}$ . The microstructure of the as-built AM 316L SS was also examined by optical microscopy and transmission electron microscopy (TEM). For TEM examination, disk specimens of 3 mm in diameter were electropolished to perforation using an electrolyte of 95% methanol and 5% perchloric acid at  $\sim -40^\circ\text{C}$ . Electropolishing of TEM disks was a challenge due to the presence of cracks and voids in the gauge section of a creep-tested specimen. Electropolished thin-foil specimens were further ion milled to obtain appreciable thin areas for TEM examination. TEM and EDS were conducted to examine dislocations, dislocation cells, subgrains, second-phase precipitates, and chemical segregations on a FEI Tecnai F20ST TEM and a FEI Talos F200X TEM in the Center for Nanoscale Materials (CNM), Argonne National Laboratory. Creep fracture mode was examined by optical microscopy.



Figure 3. Argonne's creep test systems.

Table 2. List of creep specimens and test conditions of AM 316 L SS.

Specimen ID	Build ID	Part geometry	Laser mode	Condition	Test T (°C)	Stress (MPa)
L101	20190308	0.5"φ Rod	Laser 1	As-built	650	225
L102	20190308	0.5"φ Rod	Laser 1	As-built	650	200
L103	20190308	0.5"φ Rod	Laser 1	As-built	650	175
L201	20190308	0.5"φ Rod	Laser 2	As-built	650	225
L202	20190308	0.5"φ Rod	Laser 2	As-built	650	200
L203	20190308	0.5"φ Rod	Laser 2	As-built	650	175
L1-1	20190315	0.5"φ Rod	Laser 1	As-built	600	200
L1-2	20190315	0.5"φ Rod	Laser 1	As-built	600	225
L1-3	20190315	0.5"φ Rod	Laser 1	As-built	600	250
L2-1	20190315	0.5"φ Rod	Laser 2	As-built	550	300
L2-2	20190315	0.5"φ Rod	Laser 2	As-built	550	250
L104	20190308	0.5"φ Rod	Laser 1	As-built	550	275
L204	20190308	0.5"φ Rod	Laser 2	As-built	550	275
L106	20190308	0.5"φ Rod	Laser 1	650°C/1h	550	275
L206	20190308	0.5"φ Rod	Laser 2	650°C/1h	550	275
L2-3	20190315	0.5"φ Rod	Laser 2	750°C/1h	550	275
L2-4	20190315	0.5"φ Rod	Laser 2	800°C/1h	550	275
L1-4	20190315	0.5"φ Rod	Laser 1	900°C/1h	550	275
L205	20190308	0.5"φ Rod	Laser 2	1050°C/1h	550	275

### 3. Results

#### 3.1. Creep Behavior of AM 316L SS

Figure 4 shows the creep curves in terms of creep strain as a function of time for AM 316L SS tested at 550, 600, and 650°C (“L1” refers to “Laser 1 specimen”; “L2” refers to “Laser 2 specimen”). The creep strain was calculated by dividing the extension by the initial gauge length of the specimen. The creep rupture data is plotted in Fig. 5 in terms of the creep stress vs. the rupture time. “Laser 1 specimens” and “Laser 2 specimens” showed comparable creep behavior. The batch variability between laser 1 and laser 2 was insignificant in these short-term creep tests. It was found that the creep rupture life,  $t_f$  and the creep stress,  $\sigma$  follows the relationship:

$$\sigma = \alpha t_f^{-\frac{1}{m}} \quad (1)$$

where  $\alpha$  and  $m$  are the constants. The value of  $m$  decreases with increasing temperature. All the creep tests showed a very short primary and secondary creep followed by a continued increase in creep rate until failure, and all the creep curves were dominated by accelerated creep. The minimum creep rate was achieved at the early stage of the test, typically at a creep strain of <1%.

The minimum creep rate was measured in the strain range of 0.2-0.6% for each test, and the data of the minimum creep rate is plotted as a function of the applied stress in Fig. 6. The minimum creep rate follows a power law relationship with the applied stress:

$$\dot{\epsilon}_{min} = A\sigma^n \quad (2)$$

where A is the constant. The creep elongation was calculated using the original adjusted gauge length of the reduced section of the specimen and the data are plotted in Fig. 7 as a function of the applied stress. The creep elongation under all the creep conditions falls in the range of 37-56%, and shows no clear dependence on specimen and test conditions and batch variability.

The creep rupture life data shown in Fig. 5 are replotted in Fig. 8 in a Larson-Miller plot and compared with the literature data of conventionally-made Type 316 SS [26, 27]. The Larson-Miller parameter,  $T(C+\log 10(t_f))$  was calculated using  $C = 17$  for both AM 316L SS and Type 316 SS. Type 316 SS shows better creep rupture strength than AM 316L SS. It should be noted that the carbon contents are significantly different in AM 316L SS and in Type 316 SS reported in the literature: the carbon concentration of 316L SS powder was 0.006%, while Sasikala et al reported a carbon concentration of 0.048% of Type 316 SS [26]. The data of Type 316 SS in [27] were derived from the 550°C and 600°C rupture equations developed by Oak Ridge National Laboratory, which represent the average behavior of Type 316 SS. The extremely low carbon content in AM 316L SS can be an important factor affecting the creep rupture strength, and the difference in carbon concentration between AM 316L SS investigated here and Type 316 SS reported in the literature complicates the comparison of creep properties of AM 316L SS and conventionally-made 316 SS and the understanding of the effect of the unique microstructural features of AM 316L SS on its creep response..

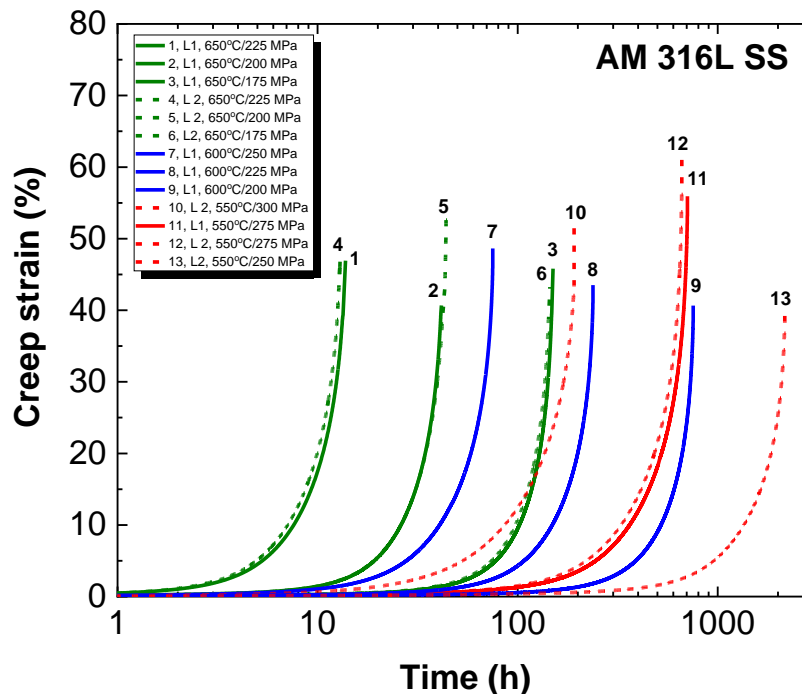


Figure 4. Creep strain as a function of time for AM 316L SS tested at 550, 600 and 650°C.

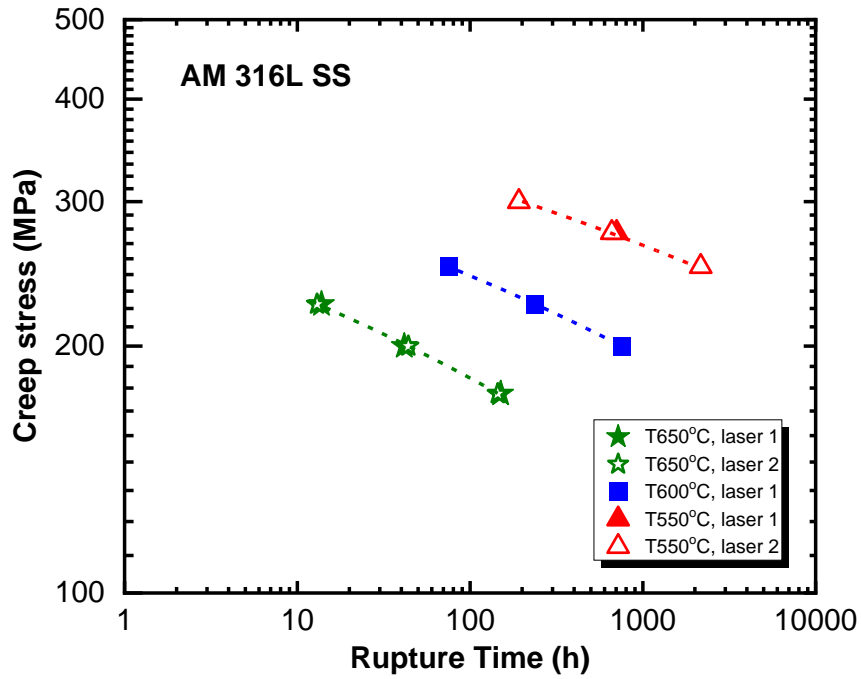


Figure 5. Stress-rupture life plot at 550, 600, and 650°C for AM 316L SS.

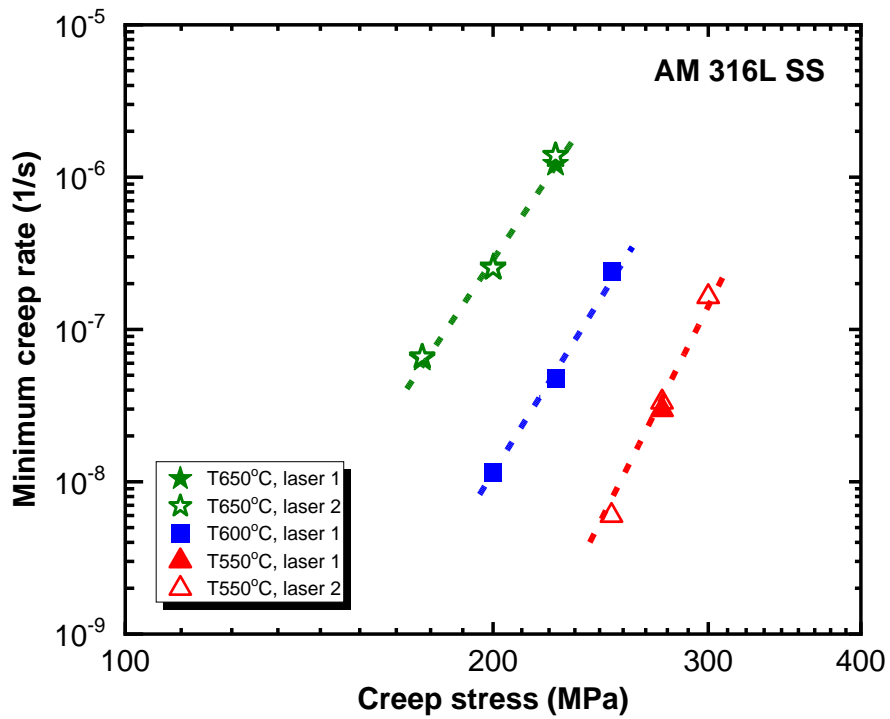


Figure 6. Minimum creep strain rates vs. creep stress for AM 316L SS tested at 550, 600, and 650°C.

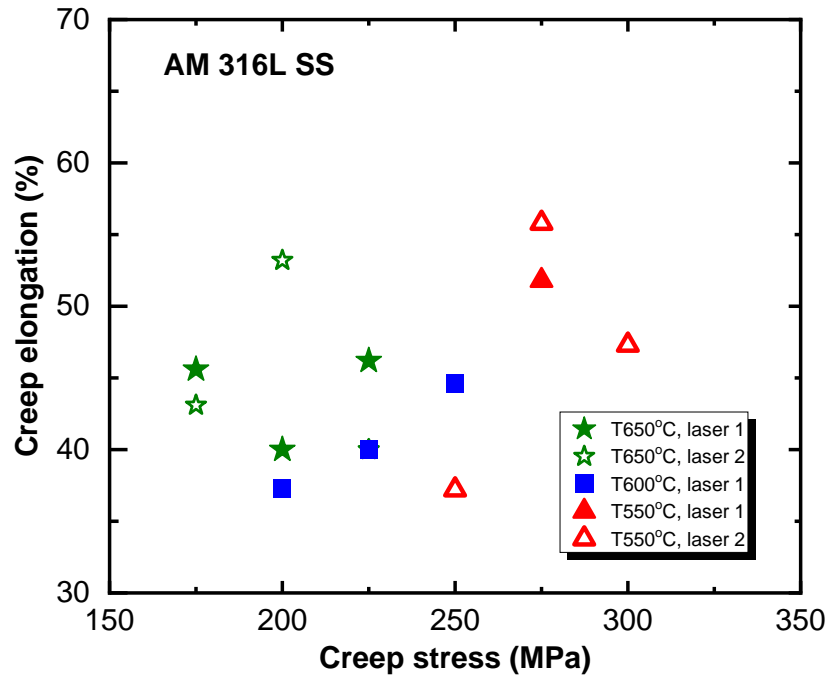


Figure 7. Creep elongation vs. creep stress for AM 316L SS tested at 550, 600, and 650°C.

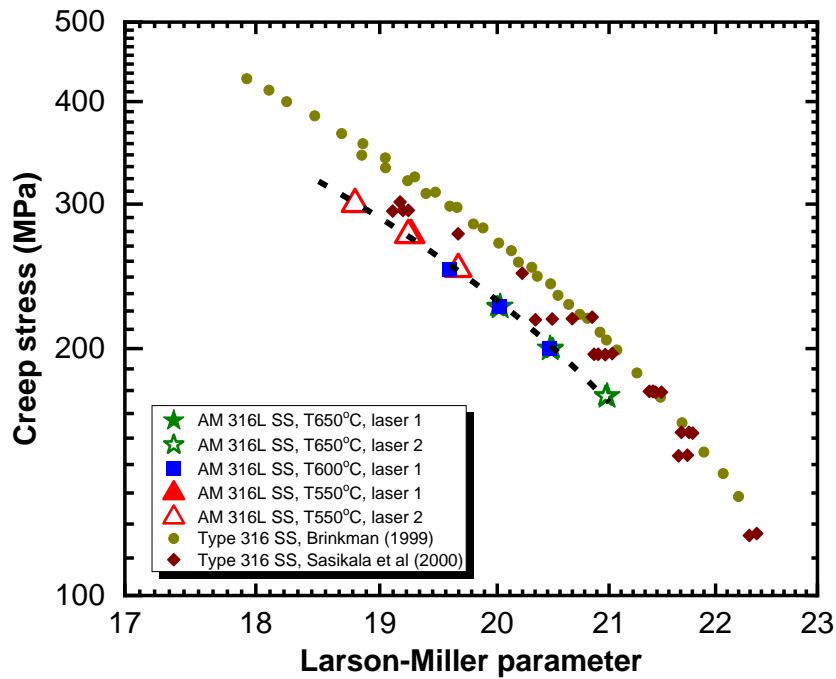


Figure 8. Larson-Miller plot for AM 316L SS tested at 550, 600, and 650°C.

### 3.2. Effect of Heat Treatment on Creep Behavior of AM 316L SS

To evaluate the effect of post-build heat treatments on the creep behavior of AM 316L SS, the heat-treated specimens were tested under the same condition, 550°C and 275 MPa, and their creep curves are compared in Fig. 9. The 650°C-heat treated specimens have longer creep lives than the specimens in the as-built and all other heat-treated conditions. All the specimens show similar creep response, exhibiting predominantly accelerated creep.

Figures 10-12 plot the creep rupture time, the minimum creep rate, and the creep elongation as a function of heat treatment temperature, respectively. The creep rupture time of AM 316L SS reached the maximum after the heat treatment at 650°C, then decreased continuously with increasing heat treatment temperature, and reached the minimum at 900°C. The 1050°C heat treatment slightly restored the creep rupture life. The minimum creep rate followed the opposite trend and reached the minimum after the heat treatment at 650°C and the maximum at 900°C. It is interesting to note that the 650°C-heat treated specimens showed the lowest creep elongations, but the longest creep lives.

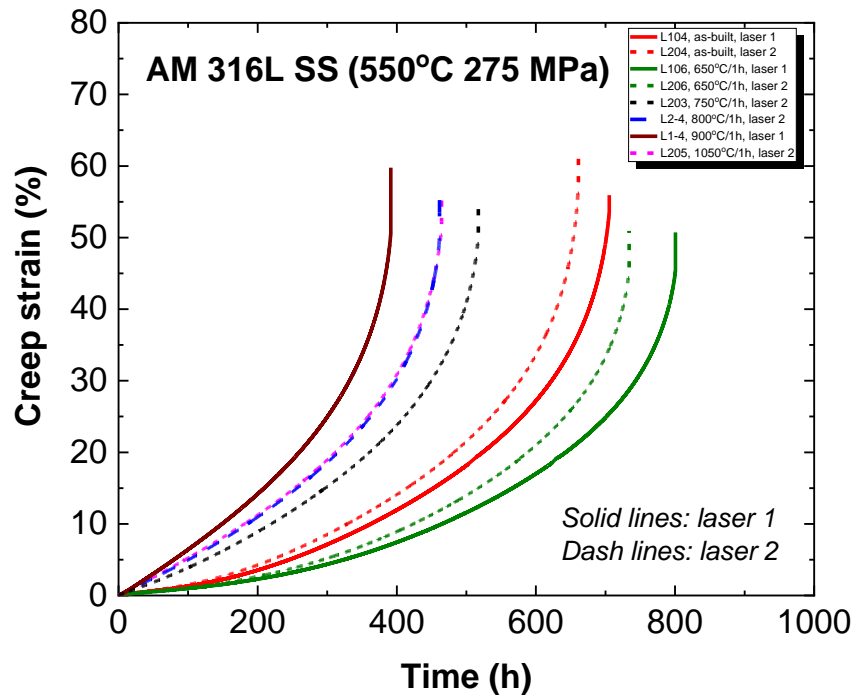


Figure 9. Creep curves of AM 316L SS heat treated at different temperatures.

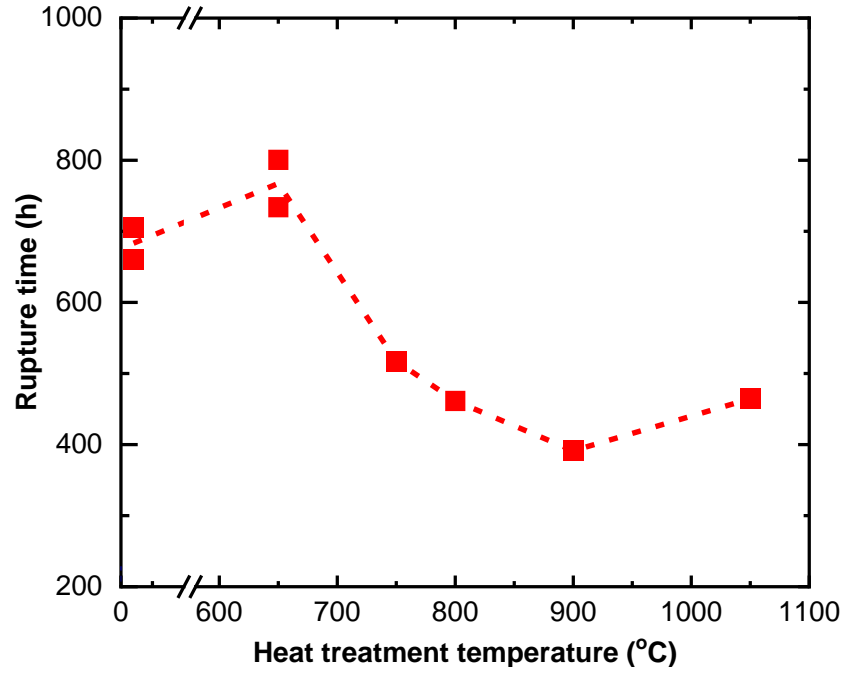


Figure 10. Effect of heat treatments on the creep rupture life of AM 316L SS tested at 550°C 275 MPa.

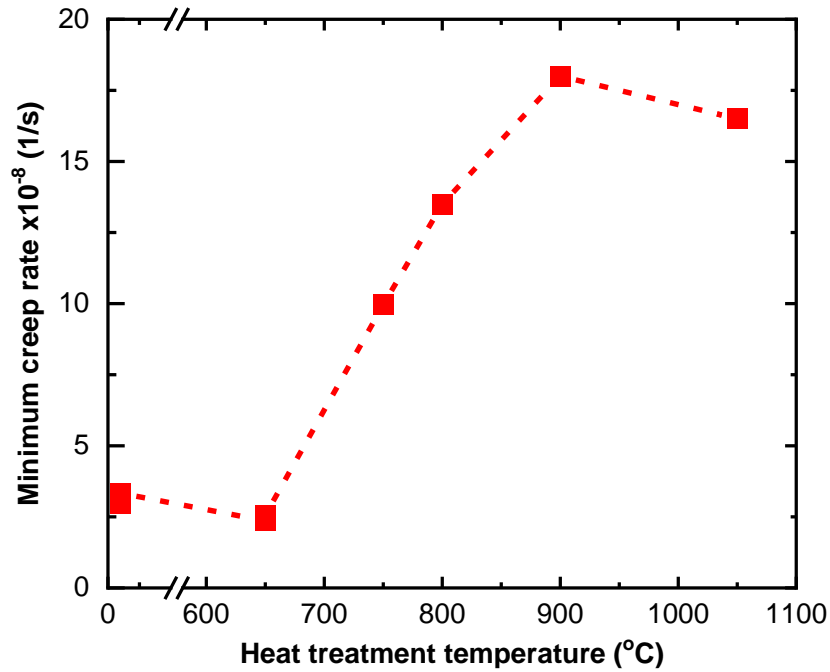


Figure 11. Effect of heat treatments on the minimum creep strain rate of AM 316L SS tested at 550°C 275 MPa.

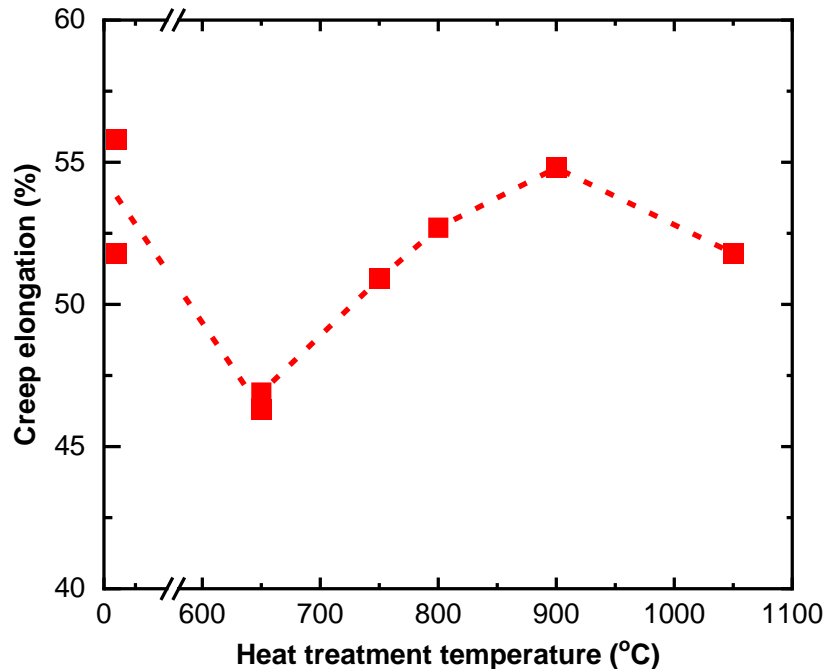


Figure 12. Effect of heat treatments on the creep elongation of AM 316L SS tested at 550°C 275 MPa.

### 3.3. Microstructure of the as-built AM 316L SS

The microstructure of the as-built AM 316L SS was examined by TEM. For TEM examination, a thin sheet (~250  $\mu\text{m}$  thick) was sectioned near the bottom end of a printed rod, and disk specimens of 3 mm in diameter were punched from the thin sheet. TEM images at various magnifications in Fig. 13(a) reveal well-organized dislocation cell structure with the mean cell size of 530 nm. The dislocation density is low inside the cells. Minimal misorientations were observed between dislocation substructures, cell walls consisted of dislocation tangles, and substructures were considered as dislocation cells. Particles were distributed both at boundaries and within cells. EDS elemental maps (Fig. 13(b)) reveal that these particles are oxides enriched in Si, Mn. The mean size of oxide particles is 25 nm. Elemental segregation was observed at cell boundaries which were enriched in Cr and Mo and depleted of Fe. These observations are consistent with the findings reported in the literature [3,28,29].

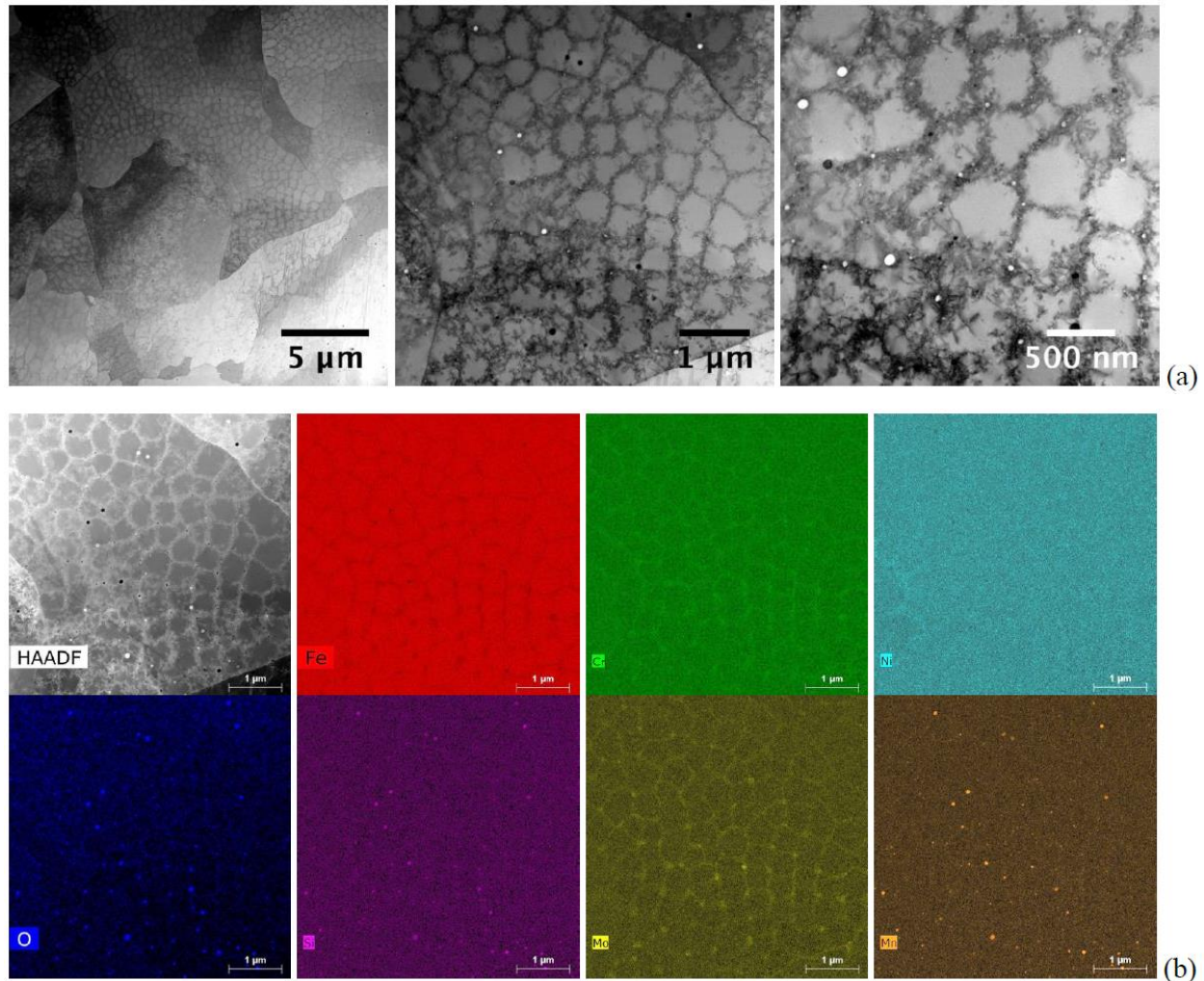


Figure 13. (a) TEM micrographs at different magnifications showing dislocation cell structure and particles; (b) HAADF micrograph and EDS elemental maps showing oxide particles and elemental segregation at boundaries in the as-built AM 316 L SS.

X-ray tomography was conducted on a creep specimen in the as-built condition prior to creep test to reveal porosity in AM 316L SS. Figure 14(a) is 3D rendering showing porosity for the entire cross section measured at the gauge midline of the creep specimen. The porosity in this volume is 0.10% with the mean size of  $7.72 \pm 0.08 \mu\text{m}$ . It should be noted that pores with size  $< 2 \mu\text{m}$  (which is the resolution limit) were not counted. Large pores were observed primarily near the centerline of the gauge and along the radial direction at specific angles. Fig. 14(b) is 3D visualization of a smaller cross-sectional area but a larger thickness in the central region of the gauge showing segregated large pores. The porosity in this smaller volume is 0.18%. Large pores have irregular shapes rather than spherical. Three main types of pores are formed during the LPBF process: (a) lack of fusion pores caused by a lack of input energy to the powder bed. Pores tend to be large and have irregular shapes; (b) keyholes pores caused by an excess of input energy during melting. Pores are large and usually circular horizontally and elongated vertically; (c) gas pores

are related to gas trapped in metal during melting and solidification, and tend to be small and have a spherical shape.

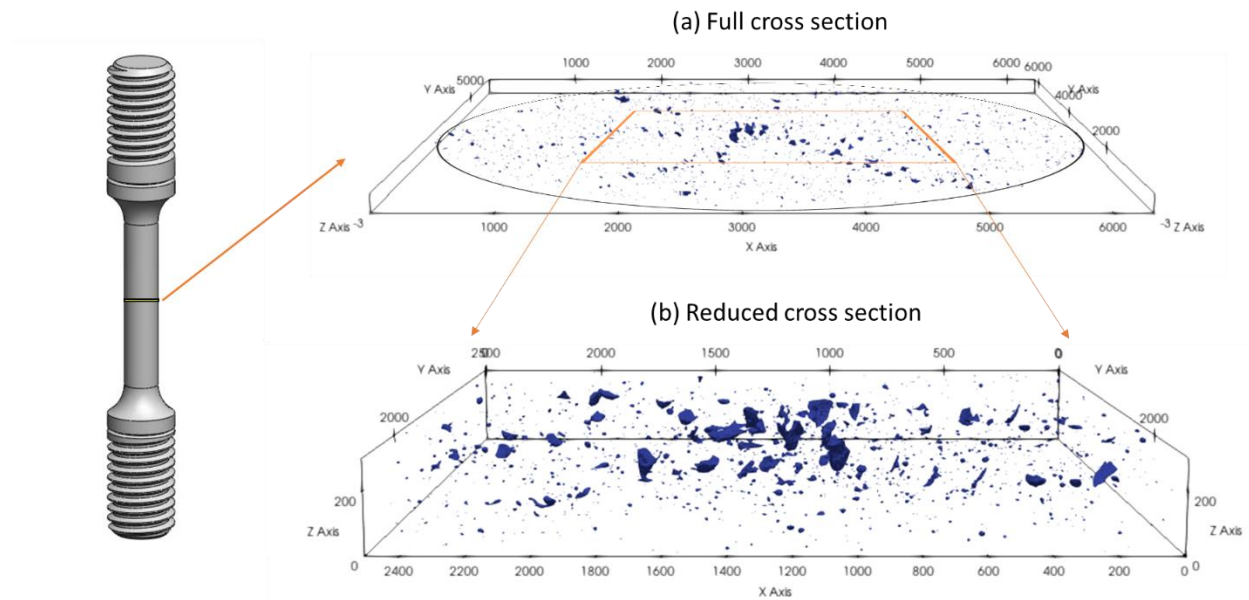


Figure 14. 3D visualization of porosity (a) the full cross section and (b) a small volume of the gauge of an AM316L SS specimen. The Z-axis is the build direction (axial label in pixel, 1 pixel = 1.172  $\mu\text{m}$ ).

### 3.4. Microstructure of Heat-Treated AM 316L SS

Figure 15 shows the microstructure of as-built AM 316L SS after thermal exposure at 650°C for 14 h. The metallographic specimen was taken from the grip section of the specimen L101 after the creep test at 650°C and 225 MPa and the specimen had a rupture life of 14 h. The specimen shows a layered structure characterized by melt pool boundaries. Within the melt pool, columnar grains grow in the build direction, as shown in the axial view of Fig. 15. The grain size in the cross section is ~20-30  $\mu\text{m}$ . Defects, e.g. lack of fusion, gas pores, are evident in Fig. 15, consistent with the observation by X-ray tomography.

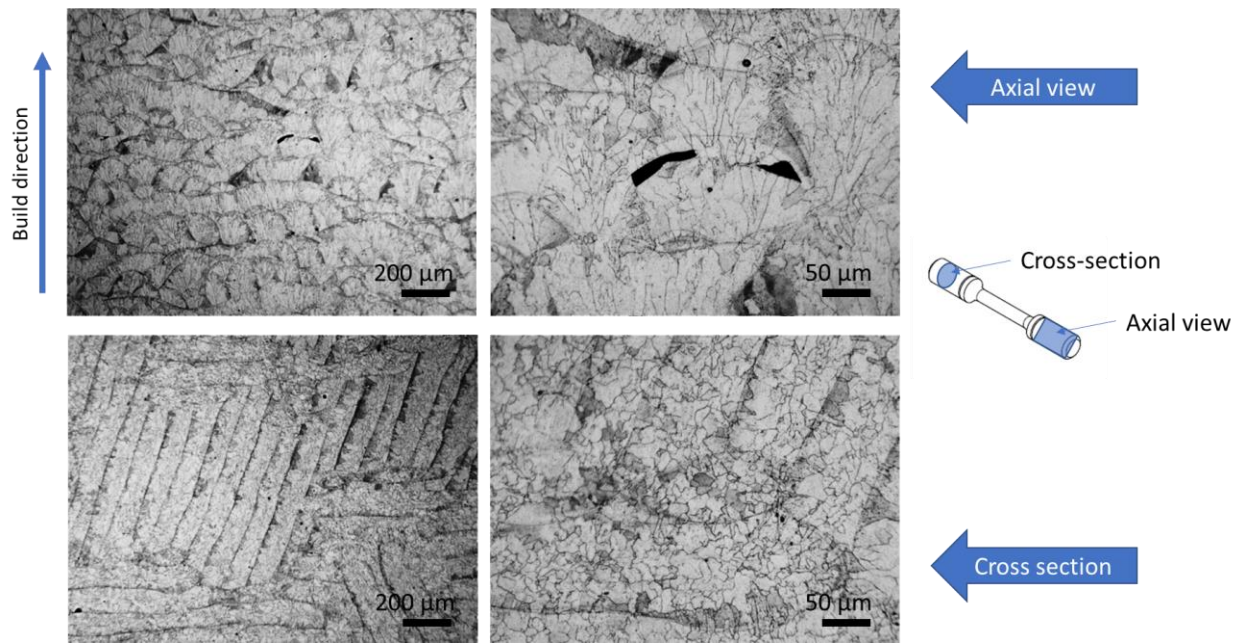


Figure 15. Optical images showing the microstructure of AM 316L SS after thermal exposure at 650°C for 14 h in the build direction (axial view) and cross section. Specimen was taken from the grip section of the creep-tested specimen L101.

Microstructure of the heat-treated specimens was examined after the creep tests at 550°C and 275 MPa by optical microscopy. Figure 16 shows optical images of the specimens heat treated at different temperatures. Metallographic specimens were taken from the grip end of the creep-tested specimen in the build direction. These specimens experienced an additional thermal exposure at 550°C during the creep test, and the thermal exposure temperature and time for each specimen are given in the parentheses in Fig. 16. It was found that thermal exposure at 550°C for 705 h (specimen L104, as-built) had a minimal effect on the microstructure of AM 316L SS. Melt pool boundaries and grain structure remained unchanged. On the other hand, melt pool boundaries are nearly invisible in the specimens heat treated at the temperature > 750°C. Melt pool boundaries are somewhat visible in the 650°C- and 750°C-heat treated specimens though they are much thinner and look more similar to grain boundaries. It should be noted that neither the 650°C/14 h nor 550°C/705 h thermal exposure can remove melt pool boundaries, as seen in Figs. 15 and 16. However, the sequential 650°C/1h and 550°C/801 h treatment indeed had a strong effect on melt pool boundaries. Ronneberg et al [30] reported that melt pool boundaries are thin bands of slightly different composition from the melt pool interior. The gradual removal of melt pool boundaries indicated an increasing influence of atomic diffusion with increasing heat treatment temperature that homogenizes the melt pool composition. Figure 16 also shows that the grain structure was not severely affected by the heat treatment below 1050°C. At 1050°C initial columnar grains started to lose their shapes, implying the occurrence of recrystallization.

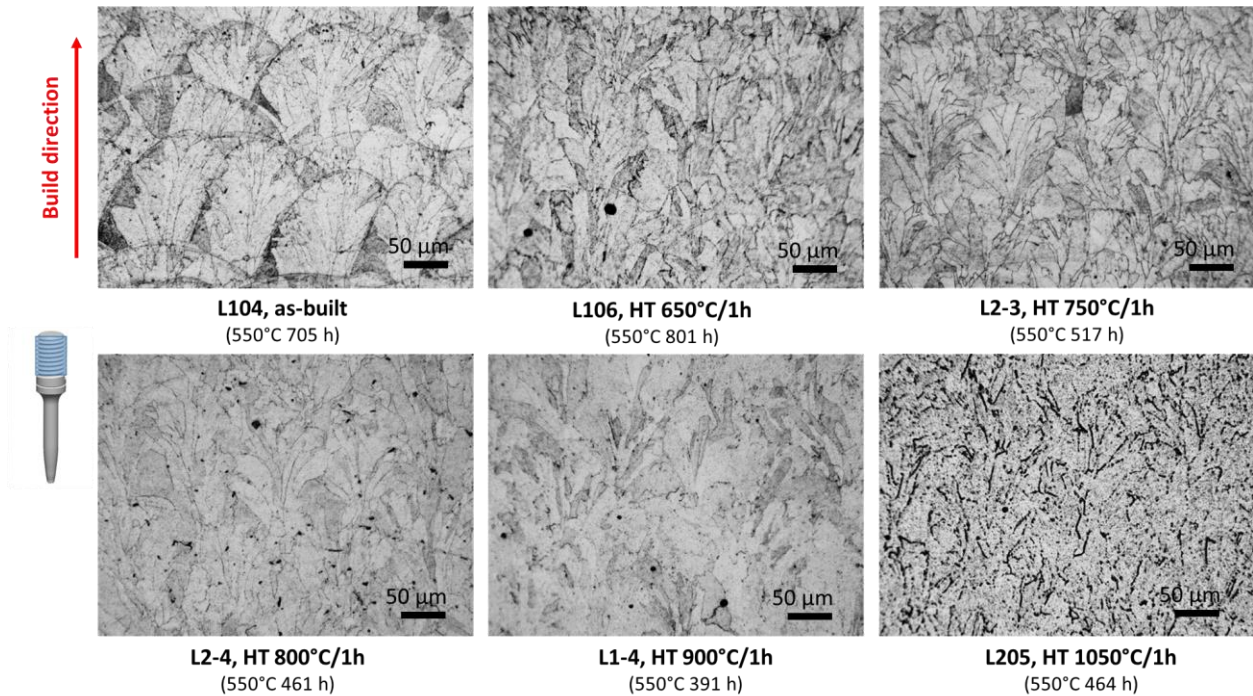


Fig. 16 Optical images showing the microstructure of heat-treated AM 316L SS in the build direction. Metallographic specimen was taken from the grip section of the creep-tested specimen. Thermal exposure condition during creep is given in the parathesis for each specimen.

The microstructure of the heat-treated specimens was also examined by TEM. Figure 17 shows TEM micrographs of the specimens heat treated at 750, 800, and 900°C, respectively. TEM disk specimens were taken from the grip section of the creep-tested specimen. Therefore, they experienced an additional thermal exposure at 550°C during the creep tests. The thermal exposure condition is given in the paratheses for each specimen in Fig. 17. Heat treatments at 750, 800 and 900°C partially removed dislocation cell structure. The remaining cells had similar sizes to that in the as-built condition. At 800 and 900°C cell boundaries became thinner and started to form a well-organized low-energy boundary of dislocation arrays instead of cell wall of dislocation tangles in the as-built condition.

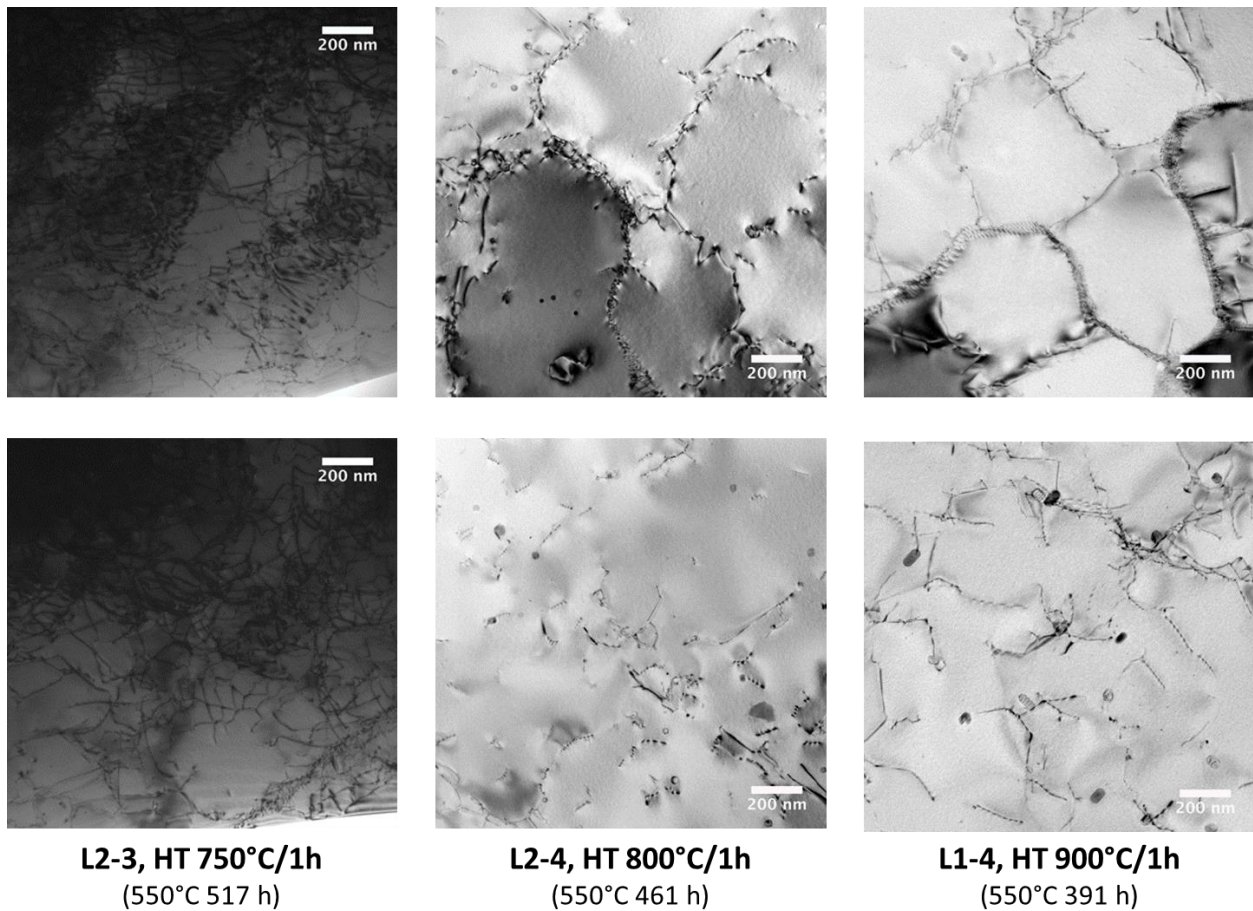


Figure 17. TEM micrographs showing the microstructure of the specimens heat treated at 750, 800, and 900°C. TEM specimen was taken from the grip section of the creep-tested specimen. Thermal exposure condition during creep is given in the parenthesis for each specimen.

The microstructure of the 1050°C-heat treated sample is shown in Fig. 18. It should be noted that the TEM specimen was taken from the grip section of specimen L105 which failed during initial loading of the creep test. Therefore, the specimen L105 experienced minimal thermal exposure after the heat treatment, and the microstructure of the TEM specimen is the effect of the heat treatment only. Unlike the heat treatments at lower temperatures, the 1050°C heat treatment completely removed the dislocation cell structure. Dislocations remained inside the grains, pinned by second-phase particles. EDS mapping of the 1050°C-heat treated specimen (Fig. 19) showed that these particles are oxides enriched in Cr and Mn, which have different chemistry from oxide particles observed in the as-built specimen (Fig. 13). Besides the chemistry change, the oxide particles in the 1050°C-heat treated specimens were also larger than those in the as-built specimen. As shown in Fig. 20, the particle mean sizes are 25 nm and 87 nm in the as-built and the 1050°C-heat treated specimens, respectively. Figure 19 also shows that the 1050°C-heat treatment effectively removed solute segregations in the as-built specimen.

Fast cooling rates during the LPBF process can produce highly non-equilibrium microstructure and high residual stress. Post-build heat treatment of 650°C/1h can potentially

reduce the residual stress in the as-built specimen. As the heat treatment temperature increases, the alloy will experience recovery, homogenization, recrystallization and grain growth. As shown in Fig. 13, dislocation cell walls consist of entangled dislocations and solute segregations in the as-built condition. The enrichment of Cr and Mo at cell boundaries has a trapping effect on dislocations and can stabilize cell boundaries. When temperature increases the diffusivities of Cr and Mo became more significant and Cr and Mo atoms start to diffuse away from cell boundaries. Removal of solute segregations facilitates dislocation movements. Dislocations can reorganize or annihilate, forming low-energy boundaries and/or cells can merge to form larger cells/subgrains. At 1050°C, boundary solute segregations and dislocation cell structure were completely removed, resulting in homogenized solute distribution and uniform dislocation structure. Columnar grains observed in the as-built specimen started to lose their shape and experiences recrystallization. Cr element initially segregated at boundaries was captured by oxide particles, forming (Mn,Cr)O oxides, which are more thermodynamically stable than the (Mn,Si)O particles. The (Mn,Cr)O oxides have a strong pinning effect on dislocations as shown in Fig. 18.

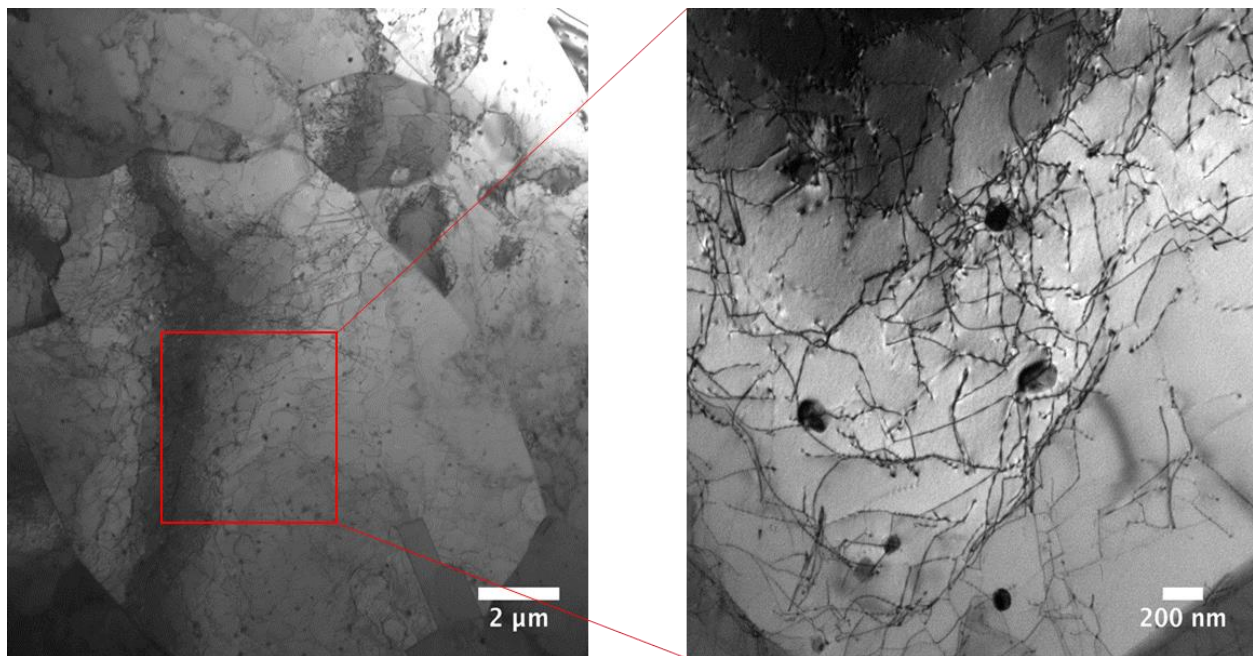


Figure 18. TEM micrographs showing the microstructure of the AM 316 L SS heat treated at 1050°C/1h.

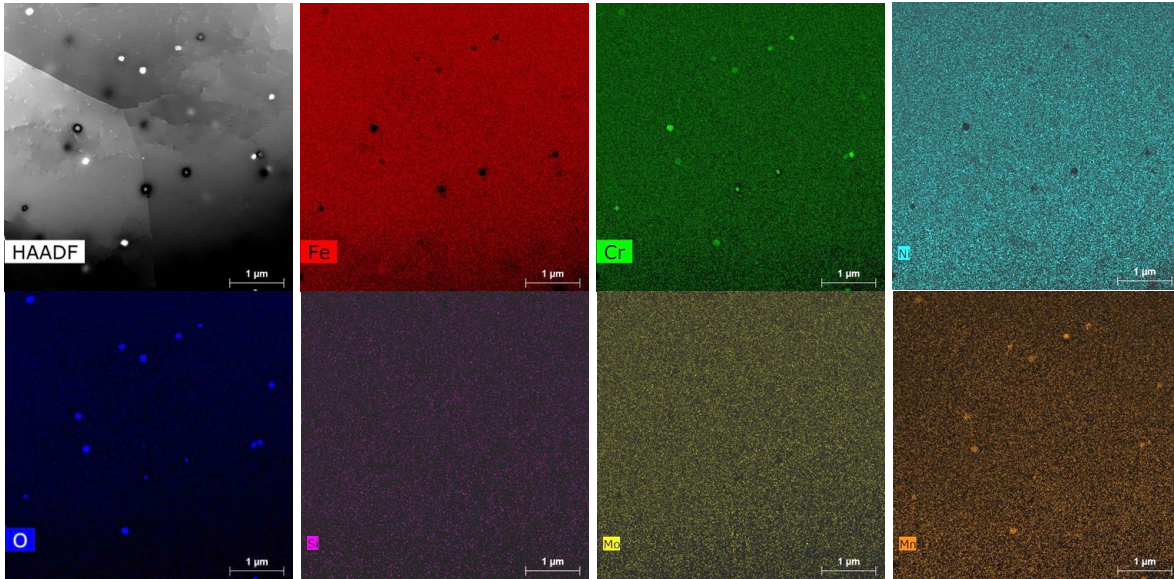


Figure 19. HAADF micrograph and EDS elemental maps of the AM 316 L SS heat treated at 1050°C/1h. The TEM specimen was taken from the grip section of specimen L205.

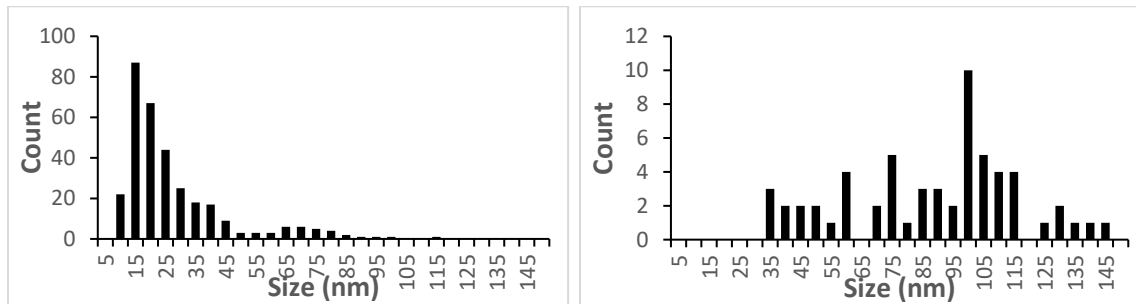


Figure 20. Particle size distributions in the as-built condition (mean size = 25 nm) (left) and in the 1050°C/1h heat treated condition (mean size = 87 nm) (right).

### 3.5. Creep-deformed microstructure of AM 316L SS

Creep damage was characterized by optical microscopy. Metallographic specimens were taken in the gauge section in the longitudinal direction. Figure 21 compares the creep-tested (550°C 275 MPa) specimens heat treated at different temperatures and in the as-built condition. It appears that specimens made from build 20190308 (L104, L106, and L205) showed a higher population of voids than specimens made from build 20190315 (L2-3, L2-4, and L1-4), though the creep elongations of these specimens do not show significant differences. Metallographic specimens were also made from the grip section of the creep-tested specimens, and optical micrographs of the unetched specimens are given in Fig. 22. There is no obvious difference in porosity between the specimens made from build 20190308 and build 20190315 that can explain the high population of creep voids observed in the specimens made from build 20190308. Further investigation is needed to understand the differences in creep void density between these specimens.

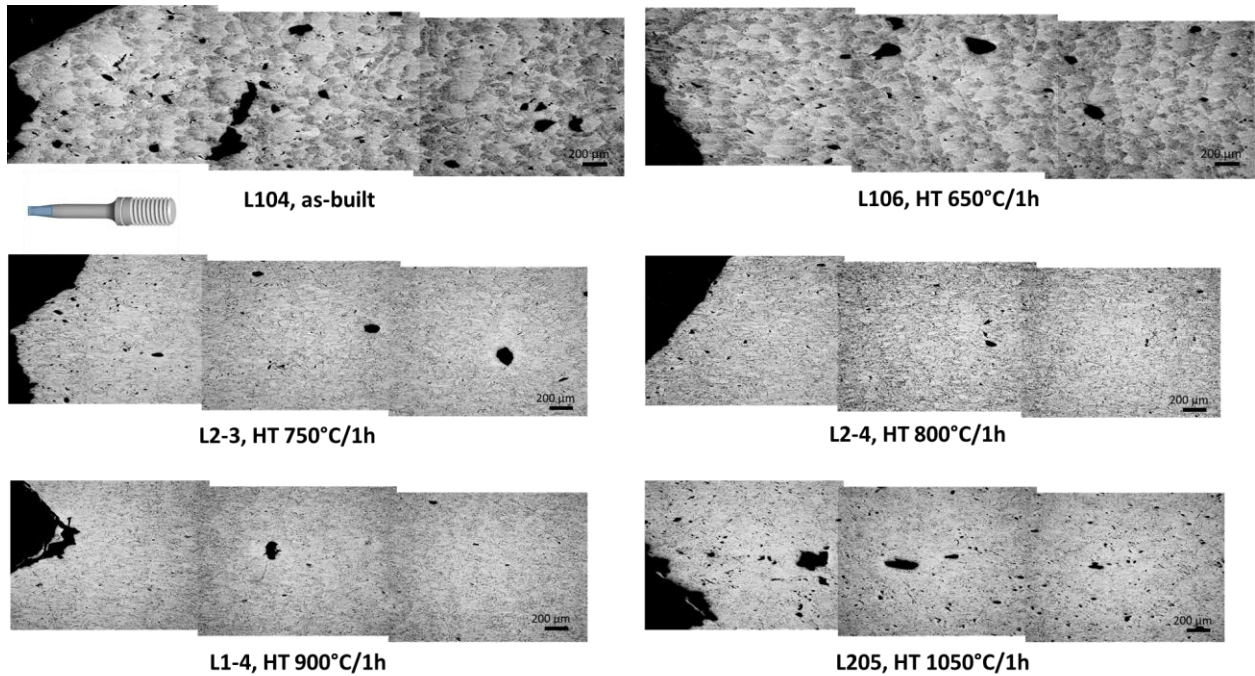


Figure 21. Low-magnification optical micrographs of the (etched) gauge section of the creep tested (550°C 275 MPa) specimens in the as-built condition or heat treated at different temperatures.

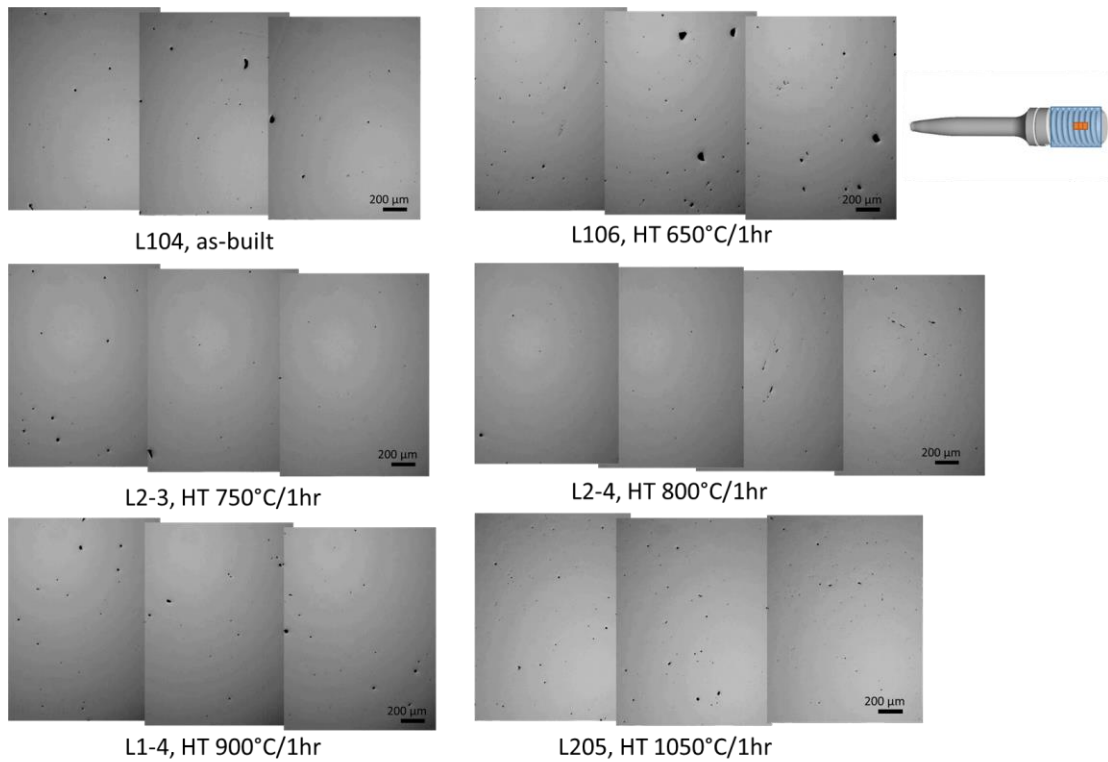


Figure 22. Optical micrographs of the (unetched) grip section of the creep tested (550°C 275 MPa) specimens in the as-built condition or heat treated at different temperatures.

High-magnification optical micrographs of the (etched) gauge section of the creep tested ( $550^{\circ}\text{C}$  275 MPa) specimens in the as-built condition or heat treated at different temperatures are shown in Fig. 23. It should be noted that optical images shown in Fig. 21 were taken after the specimen surfaces were severely etched, which manifest melt pool boundaries. The etched surfaces were subsequently lightly polished to better reveal grain boundaries, as shown in Fig. 23. Grain boundary cracking was the dominant failure mode in all the specimens. Cracks grew primarily along the grain boundaries perpendicular to the loading direction. Grains were severely distorted under creep.

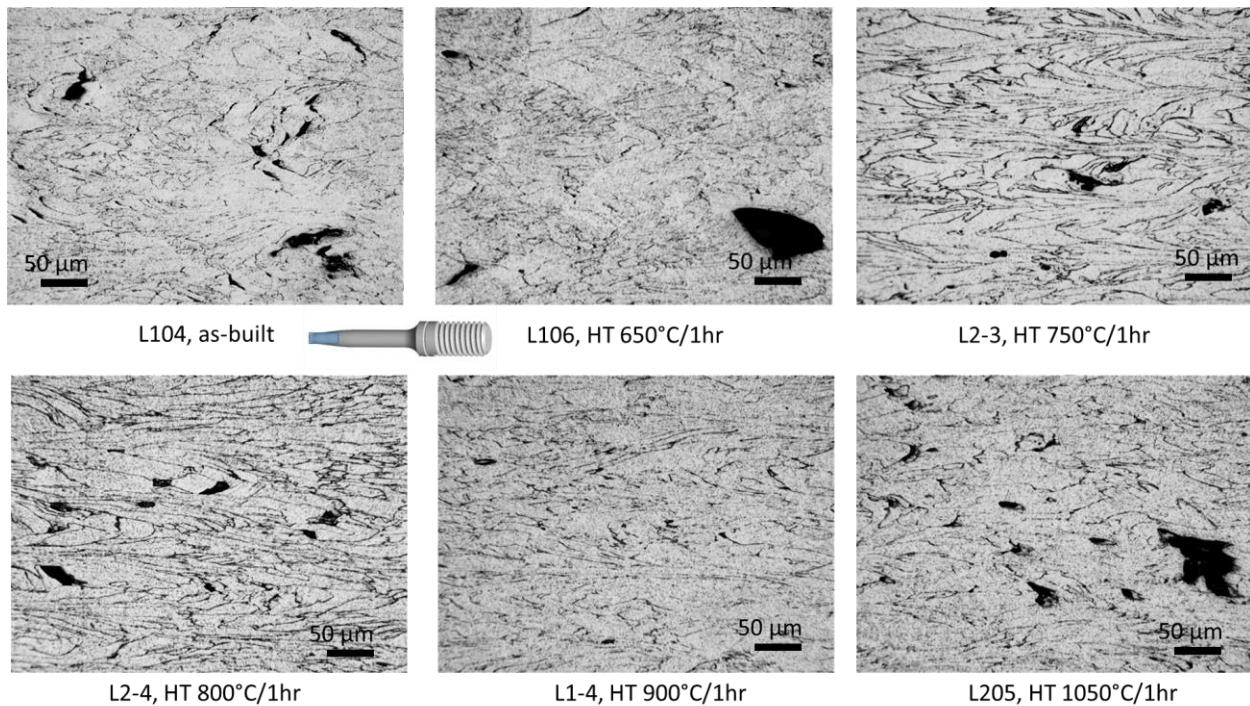


Figure 23. High-magnification optical micrographs of the (etched) gauge section of the creep tested ( $550^{\circ}\text{C}$  275 MPa) specimens in the as-built condition or heat treated at different temperatures.

Microstructure of the creep-tested specimens was also examined by TEM. TEM disk specimens of 3 mm in diameter were cut from the gauge section of a specimen away from the fracture surface of the creep-tested specimen. Figure 24 shows the microstructure of as-built AM 316 L SS after creep test at  $550^{\circ}\text{C}/275$  MPa and  $650^{\circ}\text{C}/225$  MPa, respectively. It was found that the initial dislocation cell structure in the as-built AM 316L SS gradually disappeared during creep and evolved into a uniformly-distributed high-density dislocation structure. Two AM 316L SS specimens tested in different creep conditions,  $550^{\circ}\text{C}/275$  MPa and  $650^{\circ}\text{C}/225$  MPa, show similar microstructure after creep. Residual cells were still observable in limited areas in both specimens. Kestenbach et al. [16] showed that dislocation structure varies considerably among individual grains of the same specimen under creep. Variations in the high stress specimen are highly dependent on grain orientations. The residual dislocation cell structure observed in the AM 316L SS creep specimens may be understood by the dependence of dislocation substructure on grain

orientation. It was also observed that the residual dislocation cells in the creep-tested specimens were smaller than the dislocation cells in the as-built specimen (530 nm). A mean size of 382 nm was measured in the 650°C/225 MPa specimen, and 334 nm in the 550°C/275 MPa in the limited areas studied under TEM.

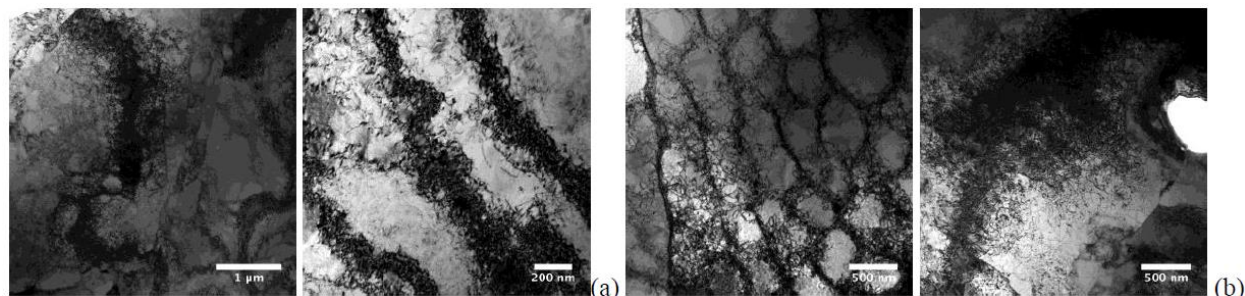


Figure 24. TEM micrographs showing the microstructure of the as-built AM 316 L SS after creep test at (a) 550°C/275 MPa and (b) 650°C/225 MPa.

#### 4. Summary

Creep tests of an additively manufactured 316L stainless steel (AM 316L SS) were conducted at temperatures of 550, 600, and 650°C and stresses between 175 and 300 MPa. Creep specimens were fabricated from rods printed by two lasers by a laser powder bed fusion process using a Concept Laser–M2 printer at Oak Ridge National Laboratory. Two builds (20190308 and 20190315) were investigated. Five different post-build heat treatments were performed at Argonne National Laboratory, namely 650°C/1h, 750°C/1h, 800°C/1h, 900°C/1h and 1050°C/1h. Creep tests of the heat-treated specimens were performed under the same test condition, 550°C and 275 MPa to evaluate and understand the effect of post-build heat treatment on the creep behavior of AM 316L SS.

These short-term creep tests showed insignificant batch variability between the specimens made by two different lasers and in different builds. All the creep curves of AM 316L SS were dominated by accelerated creep. The minimum creep rate was achieved at the early stage of the test, typically at a creep strain of <1%. The minimum creep rate – stress plot follows a power-law relationship, implying dislocation creep mechanisms. The creep rupture life of AM 316L SS was described by a Larson-Miller plot with  $C = 17$ , and AM 316LSS had a relatively shorter creep life when compared to the literature data of conventionally-made Type 316 SS.

Post-build heat treatments have a significant effect on the creep properties of AM 316L SS. The creep rupture time of AM 316L SS reached the maximum after the heat treatment at 650°C, then decreased continuously with increasing heat treatment temperature, and reached the minimum at 900°C. The 1050°C heat treatment slightly restored the creep rupture life. The minimum creep rate followed the opposite trend and reached the minimum after the heat treatment at 650°C and the maximum at 900°C. All the specimens have creep elongation > 50%.

The microstructure of the as-built AM 316L SS had a columnar grain structure with well-organized dislocation cells of the mean size of 530 nm. Oxide particles enriched in Si, Mn and

solute segregations of Cr and Mo at boundaries were observed in the as-built condition. Synchrotron X-ray tomography revealed internal porosity of 0.1% across the gauge section of the as-built specimen with large pores segregated in the center and in selected radial directions. Under creep dislocation cells in the as-built AM 316 L SS evolved into a uniform dislocation structure. Intergranular creep fracture was the dominant failure mode. Post-build heat treatment at 1050°C completely removed the dislocation cell structure and solute segregations and oxide particles were enriched in Cr, Mn and grew bigger, while heat treatments at 750, 800 and 900°C partially destroyed the dislocation cell structure with remaining cells maintaining the same size as in the as-built condition. Cell boundaries evolved from dislocation tangles to well-organized low-energy structure of dislocation arrays. Melt pool boundaries also gradually disappeared after the heat treatment and became nearly invisible at the heat treatment temperature >750°C. It is suggested that dislocation cells provided creep resistance of AM 316L SS but became unstable under creep or under post-build heat treatments. Solute segregations at boundaries play an important role in stabilizing the cell structure in AM 316L SS. Oxides in the 1050°C-heat treated specimen may have a stronger pinning effect on dislocations.

## **ACKNOWLEDGEMENT**

Work was supported by the Transformational Challenge Reactor Program funded by the U.S. Department of Energy, Office of Nuclear Energy under Contract DE-AC02-06CH11357. Materials were provided by Oak Ridge National Laboratory. Use of the Center for Nanoscale Materials, an Office of Science user facility, was supported by the U.S. Department of Energy, Office of Science, Office of Basic Energy Sciences, under Contract No. DE-AC02-06CH11357. This research used resources of the Advanced Photon Source, a U.S. Department of Energy (DOE) Office of Science User Facility operated for the DOE Office of Science by Argonne National Laboratory under Contract No. DE-AC02-06CH11357. We would like to acknowledge Chase Joslin and Ryan Duncan for specimen preparation at ORNL, Ed Listwan and David Rink for assistance with creep tests, and Peter Kenesei for assistance in X-ray tomography reconstruction at ANL. Kurt Terrani and TS Byun are thanked for providing useful direction and discussions during this effort.

## References

1. K.A. Terrani “Accelerating the Deployment of Advanced Nuclear Energy Systems.” *Nuclear News*, Apr. 2020, 34-37.
2. Z. Sun, X. Tan, S.B. Tor, C. K. Chua, “Simultaneously enhanced strength and ductility for 3D-printed stainless steel 316L by selective laser melting,” *NPG Asia Materials* 10 (2018) 127.
3. Y.M. Wang, T. Voisin, J.T. McKeown, J. Ye, N.P. Calta, Z. Li, Z. Zeng, et al., “Additively manufactured hierarchical stainless steels with high strength and ductility”, *Nature Materials* 17 (2018) 63.
4. G.T. Gray III, V. Livescu, P.A. Rigg, C.P. Trujillo, C.M. Cady, S.R. Chen, J.S. Carpenter, T.J. Lienert, S.J. Fensin, “Structure/property (constitutive and spallation response) of additively manufactured 316L stainless steel”, *Acta Materialia* 138 (2017) 140.
5. Oak Ridge National Laboratory. "Transformational Challenge Reactor," Oak Ridge National Laboratory. <https://tcr.ornl.gov/>.
6. J. Simpson, J. Haley, C. Cramer, O. Shafer, A. Elliott, W. Peter, L. Lover, R. Dehoff, “Considerations for application of additive manufacturing to nuclear reactor core components,” ORNL/TM-2019-1190, Oak Ridge National Laboratory (2019).
7. B.R. Betzler, B. J. Ade, A. J. Wysocki, P. K. Jain, P. C. Chesser, M. S. Greenwood, K. A. Terrani, “Transformational Challenge Reactor Preconceptual Core Design Studies.” *Nuclear Engineering and Design* **367** (2020) 110781.
8. R. Singh, A. Gupta, et al., “Powder bed fusion process in additive manufacturing: an overview,” *Materials Today* 26 (2020) 3058.
9. P. Bajaj, A. Hariharan, A. Kini, P. Kurnsteiner, D. Raabe, E. A. Jagle, “Steels in additive manufacturing: a review of their microstructure and properties,” *Mater. Sci. & Eng. A* 772 (2020) 138633.
10. K. Saeidi, X. Gao, Y. Zhong, Z.J. Shen, “Hardened austenite steel with columnar sub-grain structure formed by laser melting,” *Mater. Sci. Eng. A* 625 (2015) 221–229.
11. E. Yasa, J.-P. Kruth, “Microstructural investigation of selective laser melting 316L stainless steel parts exposed to laser re-melting,” *Proc. Eng.* 19 (2011) 389–395.
12. O. Salman, C. Gammer, A. Chaubey, J. Eckert, S. Scudino, “Effect of heat treatment on microstructure and mechanical properties of 316L steel synthesized by selective laser melting,” *Mater. Sci. Eng. A* (2019).
13. Y. Zhong, L. Liu, S. Wikman, D. Cui, Z. Shen, Intragranular cellular segregation network structure strengthening 316L stainless steel prepared by selective laser melting, *J. Nucl. Mater.* 470 (2016) 170–178.
14. V. K. Lindroos & H. M. Miettinen (1967) The structure and formation of dislocation networks in aluminium-magnesium alloys, *Philosophical Magazine*, 16:141, 593-610.
15. J.R. Foulds, J. Motteff, V.K. Sikka, J.W. McEnerney, “Deformation behavior of a 16-8-2 GTA weld as influenced by its solidification substructure,” *Metall. Trans. A* 14A (1983) 1357.
16. H.J. Kestenbach, W. Krause, T.L. da Silveira, “Creep of 316 stainless steel under high stresses,” *Acta Metall.* 26 (1978) 661.
17. K.D. Challenger and J. Motteff, “Quantitative characterization of the substructure of AISI 316 stainless steel resulting from creep,” *Metall. Trans.* 4 (1973) 749.
18. H.J. Kestenbach, T.L. Da Silveira, S.N. Monteiro, “On subgrain formation during creep of 316 stainless steel,” *Metall. Trans.* 7A (1976) 155.

19. K.D. Challenger and J. Moteff, "Quantitative characterization of the substructure of AISI 316 stainless steel resulting from creep," *Metall. Trans.* 4 (1973) 749.
20. L.J. Cuddy, "Internal stresses and structures development during creep," *Metall. Trans.* 1 (1970) 395.
21. Monteiro et al "Creep parameters and dislocation substructure in AISI 316 austenitic stainless steel from 600°C to 800°C," *Mater. Res.* 20 (2017) 231.
22. O.D. Sherby and P.M. Burke, *Prog. Mater. Sci.* 13 (1968) 325.
23. K.G. Field, J. Simpson, M.N. Gussev, H. Wang, M. Li, X. Chen, T. Koyanagi, K. Kane, A.M. Rossy, M. Balooch, K.A. Terrni, "Handbook of advanced manufactured material properties from TCR structure builds at ORNL – FY19," ORNL/TM-2019/1328 (2019).
24. L. Scime, D. Siddel, S. Baird, V. Paquit, Layer-wise anomaly detection and classification for powder bed additive manufacturing processes: A machine-agnostic algorithm for real-time pixel-wise semantic segmentation, *Addit. Manuf.* 36 (2020) 101453.
25. H.J. Fros and M.F. Ashby, *Deformation mechanism maps: the plasticity and creep of metals and ceramics*, Pergamon Press, 1982.
26. G. Sasikala, M.D. Mathew, K. B. S. Raom S.L. Mannan, "Creep deformation and fracture behavior of Type 316 and 316L(N) stainless steels and their weld metals," *Metall. Mater. Trans.* 31A (2000) 1175.
27. C. R. Brinkman, "Elevated-temperature mechanical properties of an advanced Type 316 stainless steel," ASME Pressure and Piping Conference, Boston, MA (US), 08/01/1999--08/05/1999.
28. S. Li, J. Ju, W. Chen, J. Yu, M. Li, Y. Wang, "Evolution of cellular dislocation structures and defects in additively manufactured austenitic stainless steel under ion irradiation," *Script Mater.* 178 (2020) 245.
29. P. Krakhmalev, et al. "Microstructure, solidification texture, and thermal stability of 316L stainless steel manufactured by laser powder bed fusion," *Metals* 8 (2018) 643.
30. T. Ronneberg, G.M. Davies, P. A. Hooper, *Materials & Design* 189 (2020) 108481.



## Nuclear Science and Engineering Division

Argonne National Laboratory  
9700 South Cass Avenue, Bldg. 401  
Argonne, IL 60439

[www.anl.gov](http://www.anl.gov)



Argonne National Laboratory is a U.S. Department of Energy  
laboratory managed by UChicago Argonne, LLC